Large-Scale Optimization Strategies for Pressure Swing Adsorption Cycle Synthesis

Alexander W. Dowling, Sree R. R. Vetukuri, and Lorenz T. Biegler
Dept. of Chemical Engineering, Carnegie Mellon University, Pittsburgh, PA 15213

DOI 10.1002/aic.13928
Published online October 15, 2012 in Wiley Online Library (wileyonlinelibrary.com).

Pressure swing adsorption (PSA) is an efficient method for gas separation and is a potential candidate for carbon dioxide (CO_2) capture from power plants. However, few PSA cycles have been designed for this purpose; the optimal design and operation of PSA cycles for CO_2 capture, as well as other systems, remains a very challenging task. In this study, we present a systematic optimization-based formulation for the synthesis and design of novel PSA cycles for CO_2 capture in IGCC power plants, which can simultaneously produce hydrogen (H_2) and CO_2 at high purity and high recovery. Here, we apply a superstructure-based approach to simultaneously determine optimal cycle configurations and design parameters for PSA units. This approach combines automatic differentiation, efficient ODE solvers for the state and sensitivity equations of the PSA model, and state of the art nonlinear programming solvers. Three optimization models are proposed, and two PSA case studies are considered. The first case study considers a binary separation of H_2 and CO_2 at high purity, where specific energy is minimized, whereas the second case study considers a larger five component separation. © 2012 American Institute of Chemical Engineers *AIChE J,* 58: 3777–3791, 2012

Keywords: pressure swing adsorption, optimization, simulation, process, mathematical modeling, green engineering

Introduction

Almost one-third of industrial CO_2 emissions are from energy conversion and power plants.[1] As CO_2 accumulation of green-house gases may seriously affect the global climate, efficient capture and storage of carbon dioxide has become an active research area. A typical goal is to capture a concentrated stream of around 90–95 vol % CO_2 for further utilization or sequestration. In an Integrated Gasification Combined Cycle (IGCC) coal-fired power plant, concentration of CO_2 occurs after gasification. CO in the syngas is oxidized to CO_2 in a water gas shift reactor, and then, the CO_2 is separated from H_2, which is eventually combusted (carbon-free) to produce electricity and steam. Among the CO_2 separation technologies to be deployed in power plants for this H_2–CO_2 separation, pressure (PSA)/vacuum swing adsorption technology offers significant advantages in terms of performance, low energy requirements, and operating costs. PSA processes achieve gas separation by exploiting affinities of gaseous components to adsorb to solid sorbents at different pressures. PSAs operate in a periodic manner by cycling through high pressure adsorption and low pressure desorption steps in packed beds. Compression and vacuum generation, therefore, constitute the key energy requirements for the process.

Several researchers have investigated the design and application of PSA systems to carbon capture separations. Schell et al.[2] characterized commercially available sorbents for pre-combustion carbon capture and proposed necessary process steps for the separation. Ho et al.[3] explored methods to reduce the cost of PSA postcombustion capture by varying design parameters with a shortcut PSA model. However, both groups do not rigorously optimize their PSA designs; thus, their systems may under-perform. Rajasree and Moharir[4] developed a strategy to optimize PSA systems using simplified process models, which are tuned to fit experimental results or more rigorous simulations. Nikolić et al.[5,6] developed a framework for optimizing PSA design. Their formulation requires a priori specification of the PSA steps (pressurization, light product purge, etc.), thus, not allowing for full system optimization.

In this study, we propose a systematic optimization-based framework to design and optimize new PSA cycles that recover H_2 (light product) and CO_2 (heavy product) at high purity and recovery. Furthermore, this framework features comprehensive partial differential algebraic equation (PDAE) bed models. As discussed in the next section, optimal designs are generated from a two-bed PSA superstructure after solving an optimal control problem (OCP). Here, we consider a detailed PDAE-based mathematical model, with a periodic boundary condition (PBC), the cyclic steady-state (CSS) equations, for the OCP. This study is an extension of earlier work, where we applied two complementary strategies to solve the OCP with PBCs. In the first approach,[7] we used direct transcription where the PDAE model was discretized in spatial and temporal domains. In the second approach,[8] a novel, Jacobian-free trust region algorithm was

Correspondence concerning this article should be addressed to L. T. Biegler at lb01@andrew.cmu.edu.

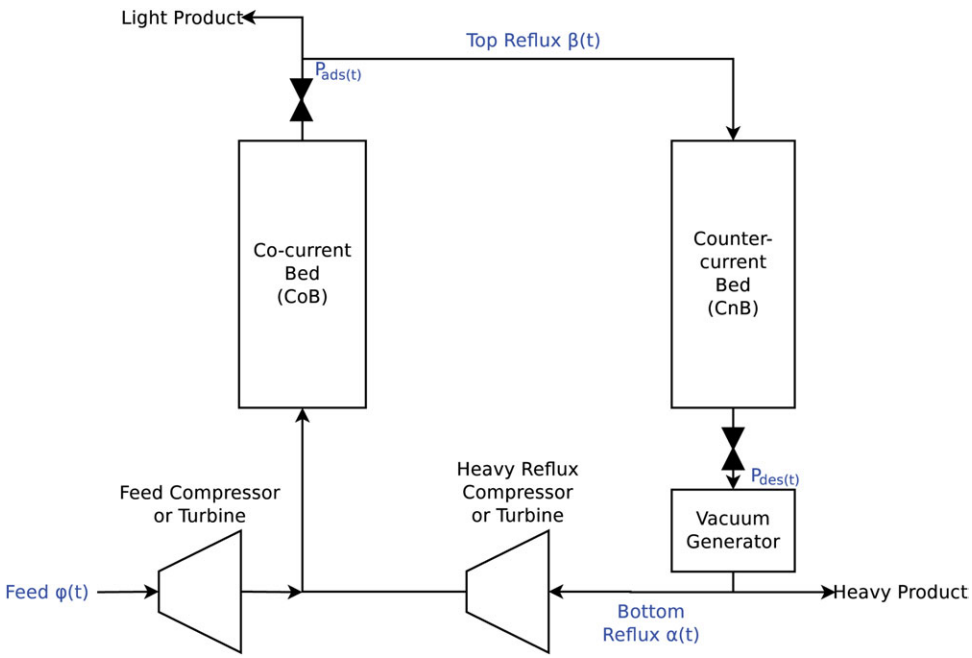

Figure 1. Two-bed PSA superstructure.[7]

[Color figure can be viewed in the online issue, which is available at wileyonlinelibrary.com.]

developed and applied to a spatially discretized OCP. A precursor of this approach has also been applied to PSA postcombustion carbon capture design.[9,10] Although both of these approaches provided successful demonstrations on this problem, further development is still needed for large, industrial-scale applications. In this study, we introduce an alternate formulation of the OCP by replacing the PBCs with sufficiently long time horizons. This has the potential to reduce the cost of the sensitivity calculation for large systems. We also use a spatial discretization approach to derive a set of ordinary differential equations (ODEs) for the OCP.

"PSA Superstructure Model" section describes the adsorption bed equations as well as the PSA superstructure for optimization. "Optimization Formulation and Solution Strategy" section then presents three nonlinear programming (NLP) formulations and outlines the solution strategy that couples a direct and adjoint sensitivity based ODE solver with the NLP solver. "PSA Optimization Results" section gives a detailed presentation of the optimal PSA cycle for a binary separation and a five component case. A brief economic analysis of the designed PSA system is also presented. "Optimization Case Studies" section then compares these optimization approaches in two PSA case studies and provides additional computational experiments to assess problem complexity. Some concluding remarks are made in the final section.

PSA Superstructure Model

Optimal PSA design requires sequencing a set of operating steps and determining the associated conditions for stream flow and pressure with each step. As described in previous work,[7] these tasks can be captured through solution of a dynamic optimization problem represented by the two-bed PSA superstructure shown in Figure 1. Here, we consider two adsorption beds: the cocurrent (CoB) and counter-current (CnB) beds. These beds determine cocurrent and counter-current operating steps in the cycle, respectively. The superstructure maintains unidirectional flow in each bed and allows the two PSA cycle beds to interact at any given time through feed and exit streams. The superstructure is designed to remove light product from the top (light end) of CoB and heavy product from the bottom (heavy end) of CnB. The bed connections are also determined by time-dependent split fractions for bottom reflux, $\alpha(t)$, and top reflux stream, $\beta(t)$. Both $\beta(t)$ and $\alpha(t)$ determine the fraction of the light product and the heavy product streams that make up the top and the bottom reflux, respectively. In addition, the time-dependent feed fraction, $\phi(t)$, determines the fraction of feed that is fed to CoB. The flue gas at pressure, P_{feed}, is further expanded or compressed, if required, and is then fed to the CoB. In addition, the CoB pressure is specified at the light (product) end by P_{ads}, whereas the pressure at the other end of the bed, P_{a}, is determined from the pressure drop in this bed. The velocity v_{a}, concentration for ith component $C_{\text{a},i}$, and temperature T_{a} at the light end of the CoB are determined from the outlet flux. Similarly, the CnB pressure is specified at the heavy end by P_{des}, while $C_{\text{d},i}$, T_{d} are tracked as state variables. v_{d} is obtained from a bed pressure drop equation and is used to calculate the output flux of the bed. P_{d} at the other end is obtained from the pressure drop in the CnB. The superstructure also incorporates compressor, vacuum generator, and valve equations to effect the pressure levels in the beds.

The superstructure model allows a wide variety of operating steps to be described by varying the control variables $\alpha(t)$, $\beta(t)$, $\phi(t)$, $P_{\text{ads}}(t)$, and $P_{\text{des}}(t)$. As we have two beds in the superstructure, half of the operating steps are realized from the CoB and half from the CnB. Thus, only

Table 1. PSA Model Equations

Component mass balance

$$\varepsilon_b \frac{\partial C_i}{\partial t} + (1-\varepsilon_b)\rho_s \frac{\partial q_i}{\partial t} + \frac{\partial (vC_i)}{\partial x} = 0 \qquad \in \{H_2, CO_2, CH_4, N_2, CO\} \quad (1)$$

LDF equation

$$\frac{\partial q_i}{\partial t} = k_i (q_i^* - q_i) \quad (2)$$

Energy balance

$$\begin{aligned} &\left(\varepsilon_t \sum_i C_i (C_{pg}^i - R) + \rho_s C_{ps}\right)\frac{\partial T}{\partial t} - \rho_s \sum_i \Delta H_i^{ads} \frac{\partial q_i}{\partial t} + \frac{\partial (vh)}{\partial x} \\ &\quad + U_A (T - T_w) = 0 \\ &C_{pg}^i = a_c^i + b_c^i T + c_c^i T^2 + d_c^i T^3 \\ &h = \sum_i \left(C_i \int C_{pg}^i \, dT\right) \end{aligned} \quad (3)$$

Dual-site Langmuir isotherm

$$\begin{aligned} &q_i^* = \frac{q_{1i}^s b_{1i} C_i RT}{1 + \sum_j b_{1j} C_j RT} + \frac{q_{2i}^s b_{2i} C_i RT}{1 + \sum_j b_{2j} C_j RT} \\ &q_{mi}^s = k_{mi}^1 + k_{mi}^2 T \qquad b_{mi} = k_{mi}^3 \exp\left(\frac{k_{mi}^4}{T}\right) \qquad m = 1,2 \end{aligned} \quad (4)$$

Ergun equation

$$-\frac{\partial P}{\partial x} = \frac{150\mu(1-\varepsilon_b)^2}{d_p^2 \varepsilon_b^3} v + \frac{1.75}{d_p}\left(\frac{1-\varepsilon_b}{\varepsilon_b^3}\right)\left(\sum_i M_w^i C_i\right) v|v| \quad (5)$$

Check valve equation

$$v(t,x) \leftarrow \begin{cases} \max(0, v_k(t,x)) & \text{if } k = a \text{ (CoB)} \\ \min(0, v_k(t,x)) & \text{if } k = d \text{ (CnB)} \end{cases} \quad (6)$$

$$\min(0,\xi) = -\max(0,-\xi) \quad (7)$$

$$\max(0,\xi) \approx 0.5\xi + 0.5\sqrt{\xi^2 + \varepsilon^2} \quad (8)$$

$$|\xi| \approx \sqrt{\xi^2 + \varepsilon^2} \quad (9)$$

Ideal gas equation

$$P = RT \sum_i C_i \quad (10)$$

Bed connection equations (see Figure 1)

$$F_i(t) = \phi(t) v_{feed} C_{feed,i} + \alpha(t)(-v_d(t)) C_{d,i}(t) \quad (11)$$

$$TR_i(t) = \beta(t) v_a(t) C_{a,i}(t) \quad (12)$$

$$LP_i(t) = (1-\beta(t)) v_a(t) C_{a,i}(t) \quad (13)$$

$$BR_i(t) = \alpha(t)(-v_d(t)) C_{d,i}(t) \quad (14)$$

$$HP_i(t) = (1-\alpha(t))(-v_d(t)) C_{d,i}(t) \quad (15)$$

half the cycle must be simulated and optimized. A PBC is imposed by matching the final conditions of the CoB to the initial conditions for the CnB and vice versa, thus, modeling CSS-two-bed behavior. A multibed extension of this approach is described in Refs. 7,11, and 12, and optimal multibed PSA cycles based on the two-bed superstructure are constructed from the solution of the control profiles $\alpha(t)$, $\beta(t)$, $\phi(t)$, $P_{ads}(t)$ and $P_{des}(t)$. In summary, the optimal cycles are designed such that the time slots for each bed are the same and that each step is an integer multiple of the time slots. Thus, multibed configurations can be generated by stacking the optimal two-bed configurations in a staggered manner to ensure that product withdrawal and feed steps are executed continuously over the cycle.

Model equations

The conservation equations and models for the equilibrium isotherm, equations of state, thermodynamic and transport properties, and bed connection equations in the superstructure are listed in Table 1 and described in full detail in Ref. 7. The CoB and CnB models are based on ideal gas behavior with axial (but no radial) variations in temperature, pressure, and concentrations of the gases in the solid and the gas phase. Pressure drop along the beds is calculated by the Ergun equation, and adsorption equilibrium is described by the dual site Langmuir isotherm. The adsorption rate is approximated by the linear driving force (LDF) expression. In the differential mass and energy balances, the second-order term has been neglected. This is because numerical dispersion created from the numerical integration strategy is typically greater than actual dispersion in industrial size PSA units, as explained in Ref. 11.

Connectivity equations between the beds are derived through consideration of mass flux and the applicable split fraction for each stream. Novel to this work is the addition of a check valve, shown in Figure 1, to maintain one-way flow in the bed. Consider the case when P_{ads}, the adsorption pressure commanded by the optimizer, is greater than $P(x,t)_{CoB}$. When realizing this action (pressurizing the CoB), a valve would be closed at the top of the bed. Mathematically, this is accomplished with a max operator in Eq. 6; if P_{ads} is greater than $P(x,t)_{CoB}$ then $v_a(t,x)$ would become negative (via the Ergun equation), which activates $\max(0,v_a(t,x))$. Likewise a min operator is used for the CnB, where $v_d(t,x) \leq 0$ due to sign convention. The min and max operators (Eq. 8) are smoothed as shown in Ref. 13, to ensure that the model remains differentiable with respect to the controls. Without modeling this valve, the bed would reverse flow at the top.

Auxiliary equations are used to calculate performance characteristics of the cycle, as shown in Table 2. Compressor and turbine works are calculated using an ideal gas model with interstage cooling[14] and integrated over the entire cycle. Note that for a turbine (Eq. 21) must be modified such that efficiency (η^k) moves from the denominator to numerator. Selected mass fluxes are also integrated over the entire cycle to determine the amount of product produced in each stream. This information is used to calculate CO_2 purity and recovery, as shown in Ref. 12. Each integral is transformed into an ODE, which is integrated along with the differential equation bed model.

Table 2. PSA Auxillary Equations

$$\text{purity}_{H_2} = \frac{\int (1-\beta(t)) v_a(t) C_{a,H_2}(t)\, dt}{\int (1-\beta(t)) v_a(t) \sum_i C_{a,i}(t)\, dt} \quad (16)$$

$$\text{purity}_{CO_2} = \frac{\int (1-\alpha(t))(-v_d(t)) C_{d,CO_2}(t)\, dt}{\int (1-\alpha(t))(-v_d(t)) \sum_i C_{d,i}(t)\, dt} \quad (17)$$

$$\text{recovery}_{H_2} = \frac{\int (1-\beta(t)) v_a(t) C_{a,H_2}(t)\, dt}{Q_{\text{feed},H_2}} \quad (18)$$

$$\text{recovery}_{CO_2} = \frac{\int (1-\alpha(t))(-v_d(t)) C_{d,CO_2}(t)\, dt}{Q_{\text{feed},CO_2}} \quad (19)$$

$$Q_{\text{feed},i} = \int \phi(t) v_{\text{feed}} C_{\text{feed},i}\, dt \qquad i \in \{H_2, CO_2, CH_4, N_2, CO\} \quad (20)$$

$$E^k = \int \frac{v^k}{\eta^k} \left(\sum_i C_i^k \right) N_{\text{stages}}^k \; RT^k \left[\left(\frac{P_{\text{out}}^k}{P_{\text{in}}^k} \right)^{\frac{\gamma-1}{\gamma}} - 1 \right] dt \quad (21)$$
$$k \in \{\text{Compressors/Turbines}\}$$

$$E = \frac{\sum_k E^k}{\int (1-\alpha(t)) v_d(t) C_{d,CO_2}(t)\, dt} \quad (22)$$

Optimization Formulation and Solution Strategy

The control profiles for the PSA superstructure include $\alpha(t)$, $\beta(t)$, $\phi(t)$, $P_{\text{ads}}(t)$, and $P_{\text{des}}(t)$. As shown in Figure 2, these profiles are discretized in a piecewise constant manner over N_{slot} time periods and treated as decision variables p in the optimization problem, along with the step (slot) times (t_s) and bed dimension (L_{bed}). Combining these profiles with the superstructure model leads to the following optimization problem.

$$\begin{aligned} \min \quad & \Phi(\bar{z}(x,t_f),p) \\ \text{s.t.} \quad & F\left(\frac{\partial \bar{z}}{\partial t}, \frac{\partial \bar{z}}{\partial x}, \bar{z}(x,t), \bar{z}(x,0), p\right) = 0 \\ & g(\bar{z}(x,t),p) \geq 0 \\ & 0 \leq (\alpha_N, \beta_N, \phi_N) \leq 1 \\ & b_L \leq (P_{\text{ads},N}, P_{\text{des},N}, \bar{p}) \leq b_U \\ & p = [\alpha_N, \beta_N, \phi_N, P_{\text{ads},N}, P_{\text{des},N}, t_s, L_{\text{bed}}] \end{aligned} \quad (23)$$

Here $\Phi(\bullet) = E$ is the objective function, which corresponds to specific energy consumed for the capture operation (kW h per tonne of CO_2 captured). $F(\bullet)$ represents the PDAE-based superstructure model for beds CoB and CnB, along with the bed connection equations and the conditions $z(x, t_0)$.

The inequality constraints $g(\bullet)$ correspond to maintaining product purity ($g_{\text{pur}} \geq 0$ corresponds to $\text{purity}_{CO_2} - 92\% \geq 0$) and recovery ($g_{\text{rec}} \geq 0$ corresponds to $\text{recovery}_{CO_2} - 90\% \geq 0$). Integral formulas to calculate these constraints are given in Table 2. Finally, we impose bounds on the decision

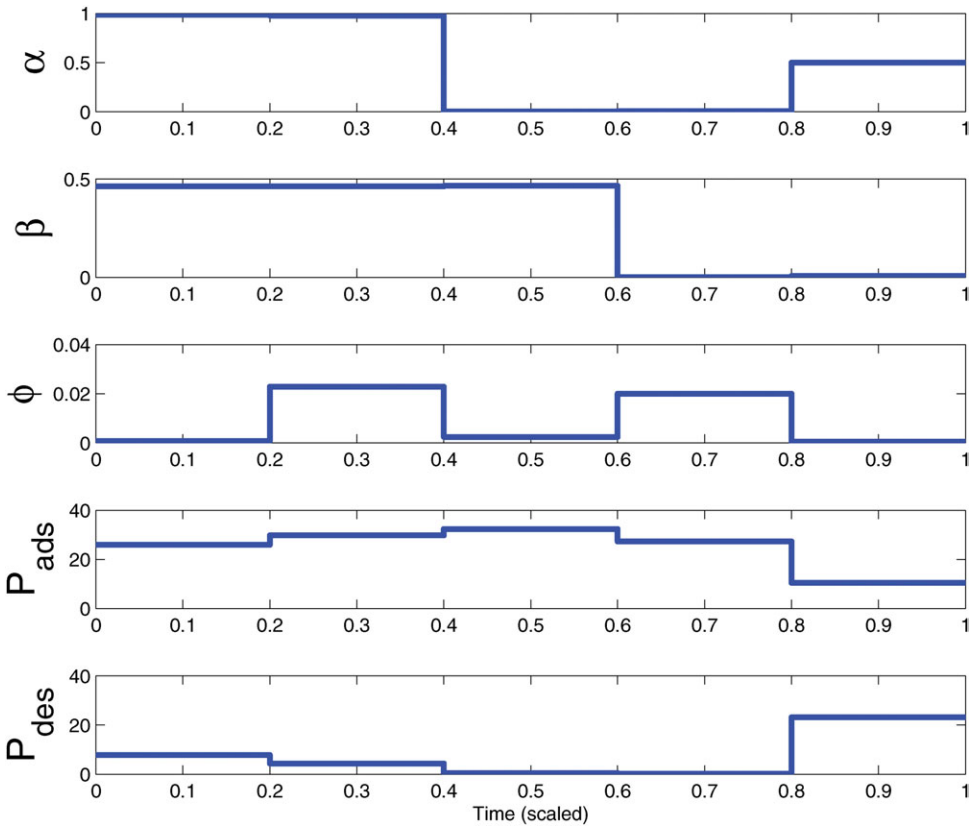

Figure 2. Discretization of control profile variables.

[Color figure can be viewed in the online issue, which is available at wileyonlinelibrary.com.]

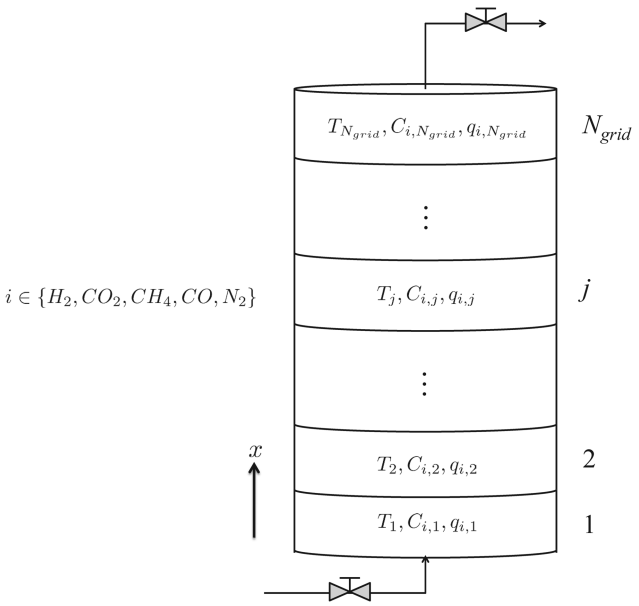

Figure 3. Discretization of column length using a finite volume method.

variables p. The discretized control variables α_N, β_N, and ϕ_N are fractions bounded between 0 and 1. Other control variables, $P_{\text{ads},N}$ and, $P_{\text{des},N}$, and remaining decision variables $\bar{p}$ are bounded between their respective bounds b_{L} and b_{U}.

Numerical integration

We solve Eq. 23 in a nested manner with repeated solution of the PDE model. Unfortunately, there is no cheap solution to the nonlinear PSA superstructure model. For the numerical solution of the bed equations, we apply a spatial, finite volume discretization of the PDE model (see Ref. 15) to obtain a system of ODEs, represented as

$$\frac{dz}{dt} = f(z, p, t), \quad z(0) = z_0 \tag{24}$$

where the state vector $z(t)$ results from the finite volume discretization of $\bar{z}(x, t)$ for the PDE model in Table 1. This discretization is also illustrated in Figure 3. We use a modified (smoothed) second-order van Leer flux limiter adapted by Jiang[11] to approximate derivatives in the system of ODEs, as shown in Eq. 25.

$$\frac{\partial(z_j v_j)}{\partial x} \approx \frac{z_{j+1/2} v_{j+1/2} - z_{j-1/2} v_{j-1/2}}{\Delta x} \tag{25}$$

The values of the states z at the walls of each finite volume $j = 1,\ldots,N_{\text{grid}}$ ($z_{j+1/2}$, $z_{j-1/2}$) are estimated using the modified van Leer flux limiter, as shown in Eqs. 26–29.

$$\begin{aligned} r &= \frac{z_j - z_{j-1}}{z_{j+1} - z_j}, \quad \text{if } v_{j+1/2} \geq 0 \\ r &= \frac{z_{j+1} - z_{j+2}}{z_j - z_{j+1}}, \quad \text{if } v_{j+1/2} < 0 \end{aligned} \tag{26}$$

$$r' = 0.5(r^2 + \varepsilon^2)^{0.5} + 0.5r \approx \max(0, r) \tag{27}$$

$$\varphi(r') = \frac{2r'}{1 + r'} \tag{28}$$

$$\begin{aligned} z_{j+1/2} &= z_j + \frac{z_{j+1} - z_j}{2}\varphi(r'), \quad \text{if } v_j \geq 0 \\ z_{j+1/2} &= z_{j+1} + \frac{z_j - z_{j+1}}{2}\varphi(r'), \quad \text{if } v_j < 0 \end{aligned} \tag{29}$$

The flux limiter is based on the ratio of successive gradients, r. This ratio is smoothed (r') to maintain differentiability. When the integrator encounters a very stiff region, such as a shock wave, $\varphi(r')$ becomes small, thus deactivating higher-order behavior. This enables sharp adsorption fronts to be accurately captured, while minimizing unrealistic oscillations, numeric dispersion and smearing (dampening). The check valve ensures one-way flow in the beds, allowing for Eq. 26 to remain the same over the entire cycle. If a flow reversal occurred, the flux limiter equations would also need to flip direction.

The system (Eq. 24) is solved with a backward difference formula integration code, CVODES.[16] CVODES is also used to solve the direct and adjoint sensitivity equations for the subsequent optimization. In addition, we used the ADOL-C code[17] to provide the Jacobian of the differential equation system during the solution step.

To enforce the CSS condition for the superstructure optimization, we explored three different optimization formulations.

PBC formulation

In our previous studies,[7,11,12] CSS operation in the PSA system was accommodated by introducing additional PBC constraints

$$h_{\text{pbc}}(\bullet) = \begin{bmatrix} \bar{z}_{\text{CoB}}(x, 0) - \bar{z}_{\text{CnB}}(x, t_{\text{f}}) \\ \bar{z}_{\text{CnB}}(x, 0) - \bar{z}_{\text{CoB}}(x, t_{\text{f}}) \end{bmatrix} \tag{30}$$

discretizing $\bar{z}(x, t)$ using the finite volume approach mentioned earlier, and imposing Eq. 30 at the spatial discretization points. Here, $t_{\text{f}} = N_{\text{slot}} \times t_{\text{s}}$ represents the cycle time of the PSA system, which is often chosen as a decision variable. For each differential state ($z^{(l)}(t)$), an additional decision variable ($z_0^{(l)}$) is introduced to represent its (unknown) initial condition. In addition to the state equations (Eq. 24), we construct and solve the sensitivity equations (Eq. 31) for $S(t) = \left(\frac{\partial z}{\partial p}\right)^T$ and provide accurate derivatives (Eq. 32) for the optimization. In our implementation, ADOL-C is used to calculate the Jacobian matrices in Eq. 31.

$$\frac{dS}{dt} = \frac{\partial f}{\partial z}^T S(t) + \frac{\partial f}{\partial p}^T, \quad S(0) = \frac{\partial z_0}{\partial p}^T \tag{31}$$

$$\nabla_{\text{p}}\psi = S(t_f)^T \frac{\partial \psi}{\partial z} + \frac{\partial \psi}{\partial p} \tag{32}$$

where $\psi = [\Phi, g_{\text{pur}}, g_{\text{rec}}, h_{\text{pbc}}]^T$ and $p = [u_1,\ldots, u_{N_{\text{slot}}}, t_{\text{s}}, L_{\text{bed}}, z_0^{(1)},\ldots,z_0^{(N\text{states})}]^T$. Relating the decision variables to the sensitivity equations, we consider the two-bed superstructure with N_{grid} spatial points and N_{comp} gas components. Each spatial point contains two differential states per component (gas concentration and sorbent loading) along with one state for temperature, as shown in Figure 3. In addition, the decision vector p contains five superstructure profile variables, with N_{slot} control slots, plus two system decision variables. This leads to $N_{\text{states}} = 2\,N_{\text{grid}}\,(2N_{\text{comp}} + 1)$ state equations and $N_{\text{cntrl}} = 5\,N_{\text{slot}} + 2$ control variables. In addition, decision variables for the N_{state} initial conditions add to the total number of optimization variables ($N_{\text{opt}} = N_{\text{cntrl}} + N_{\text{state}}$). There are also $N_{\text{aux}} = 12$ auxillary differential equations (Table 2) to

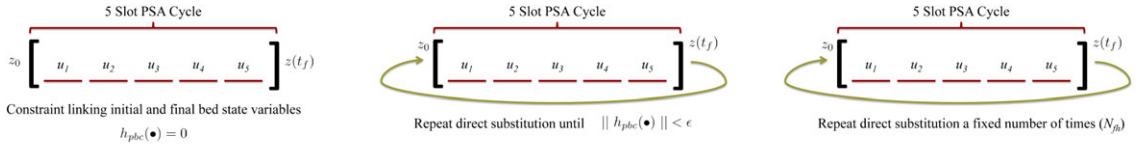

(a) PBC (b) DFO (c) FH

Figure 4. Illustrations of the three formulations to handle CSS conditions.

[Color figure can be viewed in the online issue, which is available at wileyonlinelibrary.com.]

calculate accumulated mass flows and compressor duties. As the initial conditions for these equations are all zero, no additional optimization variables are associated with them. Ultimately, this leads to $N_{sens} = (N_{state} + N_{aux})\, N_{opt}$ sensitivity equations. In particular, for the relatively small problem considered here ($N_{grid} = 11$, $N_{comp} = 2$, and $N_{slot} = 5$), we already have 16,714 direct sensitivity equations. For $N_{comp} = 5$, this increases to 68,326 sensitivity equations and the solution time for the sensitivity equations (which are evaluated for each optimization iteration) increases from 5–10 CPU minutes to over an hour. The resulting (outer) NLP with $N_{opt} = 137$ variables is solved with IPOPT,[18] a large-scale barrier NLP solver. Because exact second derivatives were not calculated in this study, the limited memory BFGS option in IPOPT was selected. To improve the feasibility of the starting point, we simulate the beds via direct substitution to CSS for specified control variables to provide a reasonable initialization for the PBCs.

Derivative-free optimization formulation

To reduce the number of decision variables and avoid the expense of solving the sensitivity equations, we drop the CSS constraints (Eq. 30) and instead solve the ODE model and the PBC through a successive substitution approach (i.e., Picard iterations) until CSS is achieved within a small tolerance (ε_{CSS}). As a result, the PSA cycles are repeated $N_{ssi} > 100$ times and $t_f = N_{ssi} \times N_{slot} \times t_s$ depends on the number of iterations to converge the cycle.

The above approach represents the inner problem for a specific choice of decision variables p, within the nested optimization strategy. In the outer problem, the inequality constraints $g(\bullet)$ are incorporated within a quadratic penalty to form the modified objective function

$$\Phi_{pen}(p) = \Phi(p) + \rho_{pen}\left[\max\{0, g_{pur}(p)\}^2 + \max\{0, g_{rec}(p)\}^2\right] \tag{33}$$

so that only a bound constrained problem remains in the space of N_{cntrl} variables p. Because direct substitution leads to a variable number of function evaluations and, hence, inaccurate derivative calculations, we apply the derivative-free optimization (DFO) solver BOBYQA[19] to the bound constrained (outer) problem.

Finite horizon formulation

The third approach is also nested without CSS equations but uses a gradient-based method over a finite horizon (FH) with $t_f = N_{fh} \times N_{slot} \times t_s$. Here, N_{fh} is chosen based on trial calculations to be sufficiently long, so that cycle convergence can be guaranteed at the optimum solution. Note that the initial conditions z_0 remain fixed, and the optimization problem is solved in the space of the N_{cntrl} variables p. Instead of using a DFO algorithm, we apply adjoint sensitivity, and note that a given adjoint system has the same dimension as the state equations. Also, three adjoint systems are required for the objective function and the two inequalities that deal with CO_2 quality, as given by

$$\frac{d\lambda}{dt} = -\frac{\partial f}{\partial z}\lambda, \quad \lambda(t_f) = \frac{\partial \psi(t_f)}{\partial z} \tag{34}$$

$$\nabla_p \psi = \left(\frac{\partial \psi}{\partial p} + \int_0^{t_f}\left[\frac{\partial f}{\partial p}\lambda\right]dt\right) \tag{35}$$

where $\psi = [\Phi, g_{pur}, g_{rec}]^T$. As shown above, two distinctive features require special attention during implementation. First, we utilize automatic differentiation via ADOL-C to calculate the Jacobian matrices in Eqs. 34 and 35. Second, the adjoint system is a final value problem with final values ($\lambda(t_f)$) specified. To solve Eqs. 34 and 35, the differential states ($z(t)$) are integrated forward in time and stored. To avoid potentially large memory requirements, numerical integrators such as CVODES store the differential state values in memory at predetermined checkpoint times; state values between checkpoints are determined using a combination of additional forward integration and interpolation calculations. As our calculations were typically not memory bound, we disabled the checkpointing features in CVODES whenever possible to trade large RAM usage (2–8 GB) for reduced CPU time. The resulting (outer) NLP with $N_{cntrl} = 27$ variables is solved with IPOPT,[18] using the limited memory BFGS option.

These three formulations—PBC, DFO, and FH—are illustrated in Figure 4. A five slot half-cycle is used as an example, where u_1 through u_5 represent the superstructure control variables for each time slot. z_0 and $z(t_f)$ represent the state variable values at the beginning and end of the half-cycle, respectively.

PSA Optimization Results

Using the PSA superstructure model, we obtained an efficient PSA cycle for CO_2–H_2 separation for carbon capture and sequestration by minimizing the specific energy for separation and compression to 15 MPa. We enforced the Department of Energy specifications of at least 92% CO_2 purity and at least 90% CO_2 recovery via inequality constraints in the optimization problem. Feed conditions for the syngas were taken from Case 2 in Ref. 20 The PSA superstructure was further modified by adding two product compressors to accommodate CO_2 pressurization to 15 MPa and other requirements for integration with the NETL IGCC flow sheet, as shown in Figure 5. Physical properties for the activated carbon sorbent were taken from Ref. 11 All these

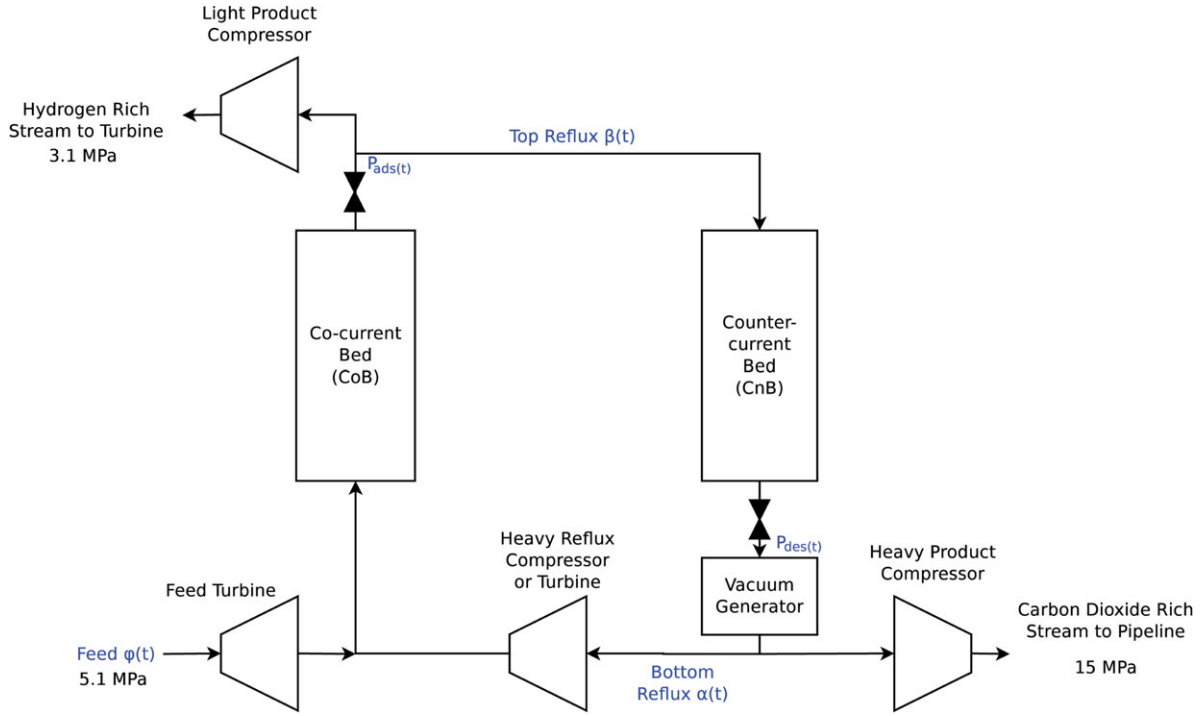

Figure 5. Superstructure with additional product compressors necessary to integrate with the IGCC flow sheet.

[Color figure can be viewed in the online issue, which is available at wileyonlinelibrary.com.]

optimization problem data, along variable bounds, are included in the Notation.

We considered both two (with CO_2 and H_2) and five component separations (with CO_2, H_2, N_2, CH_4, and CO). For both, we obtained similar energy requirements: 83.51 and 86.82 kW h per tonne CO_2 captured, respectively, for the capture process (i.e., separation and subsequent compression to 15 MPa). The specific energy usage for each compressor and turbine is shown in Table 3 for the best five component result.

The optimized cycles resulting from the case studies include heavy product purges, an infrequently utilized PSA step, to meet constraints on CO_2 purity. This demonstrates the variety of PSA steps considered by the superstructure. Furthermore, the optimized cycles produced in the case studies are all similar in the sequence of steps, although operating variables, such as pressures and flow rates, are different between solutions.

We present the best designed cycle for the five component separation (from Case Study 2B) in detail to demonstrate the realization of a PSA system from the superstructure. The optimal control profile is shown in Figure 2, and an illustration of the resultant cycle is shown in Figure 6. In the first step of this cycle, Bed A is pressurized using feed and recycle from Bed B. During the next two steps, Bed A is pressurized to 23.7 atm, whereas Bed B is independently depressurized to 0.4 atm, producing CO_2-rich product. As feed gas is passed through Bed A at 27 atm during the fourth step, CO_2 preferentially adsorbs to the sorbent, resulting in a H_2-rich product. At the same time, Bed B is further depressurized to 0.2 atm producing additional CO_2 product. During the final step, Bed A is depressurized to 10.4 atm producing additional H_2-rich product. A very small amount of product is recycled into Bed B to purge the top of the bed. After completing these five steps, both beds switch roles. Bed A becomes the desorbing bed, and Bed B becomes the adsorbing bed. The steps are also described in Table 4.

Table 5 includes a detailed numerical description of PSA system at cyclic step state. The top section of the table shows the integrated mole flows for each step of the cycle for the feed, light product, and heavy product streams. The middle section of the table shows a snapshot of moles in each bed at the beginning of each cycle. Because only a half-cycle is simulated, Beds A and B exchange roles after Step 5 in the table. Thus, values for Bed A and the first Step 1 match Bed B for the second Step 1 and vice versa. This matching demonstrates convergence to CSS. Furthermore, all the mole values in the table have been scaled such that 1.000 (scaled) mole of feed gas enters the PSA system during the half-cycle. As a consequence, mole balances are consistent throughout the table. For example, 0.7031 and 1.2909 scaled moles are present in Bed A and Bed B, respectively, at the beginning of Step 1. During Step 1, 0.017 scaled moles are feed into the system, and 0.001 scaled moles are extracted as heavy product. This results in $0.7031 + 1.2909 + 0.017 - 0.001 = 2.010$ scaled moles in the beds at the beginning of Step 2. In the table, there are $0.7908 + 1.2197 = 2.0105$ scaled moles reported at the beginning of Step 2, thus, demonstrating the overall mole balance is consistent.

Table 3. Compressor/Turbine Specific Energy

Equipment	Specific Energy (kW h/tonne CO_2)
Heavy product turbine	−3.26
Vacuum generator	12.57
Feed turbine	−35.40
CO_2 compressor	99.88
H_2 compressor	13.03
Total	86.82

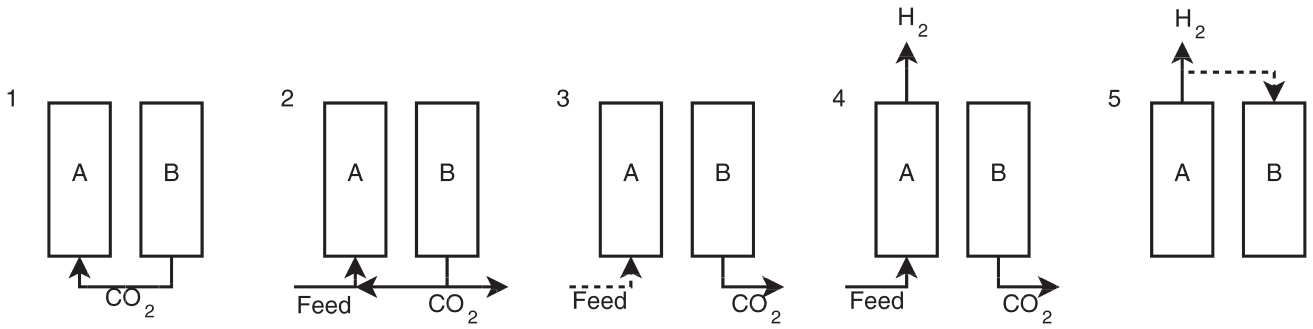

Figure 6. Optimized cycle.

Finally, the superstructure control variable values are reported in the bottom portion of Table 5. These are the same values shown in Figure 2. Note that the starred commanded pressures for $P_{ads}(P_{des})$ correspond to closed valves and zero mass flow from the outlet of CoB (CnB). This results from the control value shown in Figure 5 being closed (preventing back flow). Thus, the control valve acts as a check valve, ensuring one-way flow.

Three-dimensional visualizations of the CO_2 and H_2 mass propagation are shown in Figure 7. These plots are for the CoB half-cycle from scaled time 0 to 1. At t = 1, the beds switch roles, thus, from time 1 to 2, the plots show the CnB.

Design scale-up

Using five bed pairs, this cycle can easily be extended to a PSA system with continuous product production. The simplest arrangement of steps is shown in Table 6. During each time slot, one of the beds performs each step. Note that the superstructure does not necessarily lead to the same number of half-cycle steps and beds. Our solution is characterized by equal slot times and has 10 (2×5) slots, 9 steps, and 5 beds (similar to the 11 steps and 5 beds from Jiang et al.[11]). Note that when a given step spans more than one slot (as with the ↓ HP step in Table 6), the relationship between beds and steps changes. Such solutions can often be realized with a sufficiently large number of time slots. Moreover, with the addition of larger storage tanks, the number of beds required for continuous feed processing and product production could be reduced. Alternately, unequal times for each slot could be allowed with a least common multiple procedure for design scale-up.[7,21]

Design economics

We conducted a postoptimization analysis to approximate the cost of electricity (COE) for an IGCC plant equipped with the optimized PSA process. We used Case 2, an IGCC plant equipped with a solvent-based carbon capture system (Selexol™), from an associated NETL report[20] as the basis for our analysis. We divided the economic analysis into three tasks: first, we replaced and removed equipment from the Case 2 flow sheet to accommodate the PSA unit. Next, we estimated the cost of the PSA equipment in Table 7. Finally, we calculated the COE using same procedure as in Ref. 20 These results along with the Case 2 result from NETL are presented in Table 8.

These calculations suggest the economic potential of PSA for carbon capture in an IGCC flow sheet; however, the COE calculations do involve several assumptions. For example, the loss of hydrogen in the PSA separation is not considered in this analysis. The PSA recovers only 95% of the hydrogen, whereas the comparison Selexol process recovers 99.4%. Accounting for this hydrogen loss is not trivial, as it would require resizing and recosting of most of the power plant systems. For a simple estimate, we scaled back the combustor and steam turbine power by the hydrogen recovery from our optimized PSA cycle. This leads to a COE around \$109/MWh. This should be viewed as an upper bound, as the power systems (turbines, generators, etc.) are too large, and the capital costs need to be readjusted. Finally, these results are only with activated carbon as the sorbent. We expect advanced sorbents under development will enable higher-performance PSA separation system for carbon capture.

There are several ways to modify the optimization framework to account for the lost hydrogen. The easiest option would be to add a constraint, such as $H_2^{recovery} \geq 99.4\%$, to force the designed system to perform similar to the baseline Selexol process. Similarly, a hydrogen recovery constraint could be added and adjusted to create a Pareto curve, similar to Ref. 7. This would offer insights into the trade-off between hydrogen recovery and separation power requirements. Finally, an expression for equivalent power of the hydrogen loss could be derived and added to the objective function. We leave these proposed modifications as future work.

Finally, it is important to note these calculations involve cost correlations, which have large uncertainties. The difference between the PSA and Selexol COE is likely within the cost correlation margin of error.

Optimization Case Studies

We now consider the computational performance of the three PSA optimization formulations. In the first case study,

Table 4. Optimized Cycle Steps

Step	Bed A	Bed B
1	Pressurize by receiving heavy reflux (↑ HR)	Depressurize by supplying heavy reflux (↓ HR)
2	Pressurize by receiving feed & heavy reflux (↑ F & HR)	Depressurize by supplying heavy reflux & heavy product (↓ HR & HP)
3	Pressurize by receiving minor feed (↑ F)	Depressurize by supplying heavy product (↓ HP)
4	Maintain pressure during adsorption step (↑ F & LP)	
5	Depressurize supplying light product (↑ LP)	Pressurize with minor light product purge (↓ LP)

Table 5. Optimized Cycle Details

	Normalized, integrated mole flow during					
	Step 1	Step 2	Step 3	Step 4	Step 5	Total
Feed						
H_2	0.010	0.277	0.030	0.242	0.006	0.565
CO_2	0.007	0.206	0.022	0.18	0.004	0.420
Impurities	0.000	0.007	0.001	0.006	0.000	0.015
All species	0.017	0.49	0.053	0.429	0.010	1.000
Light product						
H_2	0.000	0.000	0.000	0.287	0.251	0.538
All species	0.000	0.000	0.000	0.291	0.297	0.589
Heavy product						
CO_2	0.001	0.002	0.286	0.090	0.000	0.378
All species	0.001	0.002	0.317	0.091	0.000	0.411
Bed A						
H_2 in gas	0.0011	0.0249	0.2473	0.2702	0.2521	0.0691
CO_2 in gas	0.0035	0.0062	0.0628	0.0705	0.1150	0.0739
Impurities in gas	0.0000	0.0002	0.0035	0.0039	0.0065	0.0030
H_2 on sorbent	0.0009	0.0175	0.1083	0.1150	0.0884	0.0243
CO_2 on sorbent	0.6974	0.7404	0.9595	0.9747	1.1066	1.1145
Impurities on sorbent	0.0003	0.0016	0.0076	0.0080	0.0117	0.0061
All species	0.7031	0.7908	1.3890	1.4424	1.5802	1.2909
Bed B						
H_2 in gas	0.0691	0.0455	0.0181	0.0000	0.0001	0.0011
CO_2 in gas	0.0739	0.0617	0.0435	0.0072	0.0034	0.0035
Impurities in gas	0.0030	0.0024	0.0015	0.0001	0.0000	0.0000
H_2 on sorbent	0.0243	0.0169	0.0074	0.0000	0.0001	0.0009
CO_2 on sorbent	1.1145	1.0877	1.0347	0.7839	0.6970	0.6973
Impurities on sorbent	0.0061	0.0054	0.0043	0.0006	0.0002	0.0003
All species	1.2909	1.2197	1.1095	0.7919	0.7009	0.7030

	Superstructure control variables during…				
	Step 1	Step 2	Step 3	Step 4	Step 5
α	0.9856	0.9776	0.0028	0.0081	0.5000
β	0.4627	0.4621	0.4653	0.0015	0.0070
ϕ	0.0008	0.0229	0.0245	0.0200	0.0005
P_{ads} (atm)	25.94*	29.74*	32.34*	27.31	10.40
P_{des} (atm)	7.79	4.33	0.42	0.13	23.09*
$t_s = 250.8$ s					$L_{bed} = 11.0$ m

Note: Moles scaled throughout table such that feed over entire cycle sums to 1.
*Commanded pressure corresponds to closed valve and zero mass flow (Figure 5.)

we compare all three formulations with a common starting point for control variables "far from a feasible solution." In this case study, we only consider two chemical species (H_2 and CO_2). The best results for each formulation are summarized in Table 10; for the PBC and FH formulations, these are rarely final solutions before termination, but instead solutions from intermediate optimizer iterations. The reported objective function values, purities, and recoveries are from simulations of the resultant control profile to CSS within tolerance $\varepsilon_{CSS} = 10^{-2}$. Termination conditions are further elaborated in Table 9. Computations were performed using an Intel i7 930 CPU (2.80 GHz) with 9 GB of RAM.

We refined the solutions obtained in Case Study 1 through an iterative process of adjusting the NLP solver settings (such as termination criteria, penalty function weight, problem scaling, and variable bounds for the DFO approach and the μ update strategy, solver tolerances, problem scaling, variables bounds, and slack variable treatment for IPOPT) and rerunning the optimization using the best known solutions as starting points. We eventually developed a starting point with a better objective function value. We used this as the common starting point for Case Study 2.

For Part A of Case Study 2, we considered only two components (H_2 and CO_2). These results are shown in Table 11. In Part B, we considered the main components (H_2 and CO_2) along with three additional trace components (N_2, CH_4, and CO). These results are summarized in Table 12. For each approach, optimizer settings were chosen based on our experience and are shown in Table 15. Table 16 contains additional data used in the case studies.

On the other hand, the DFO approach had the least favorable performance of the three optimization formulations and was prone to termination far from the optimum. In Case Studies 1 and 2A, the DFO formulation terminated with a substantally larger objective function value than the other two approaches. In Case Study 2B, the DFO approach terminated at a solution with both a large objective function value and infeasible CO_2 purity and recovery values. This is due in part to the penalty function used to incorporate the two CO_2 specification constraints; there is no mechanism to enforce problem feasibility directly. We were able to find feasible solutions with the DFO approach for only some of the considered starting points. This could only be done with careful adjustment of the optimizer settings, gradually increasing the penalty term and then restarting the optimization algorithm from the previous solution. Due to the absence of derivatives and tight termination criteria, many iterations were required for the optimization algorithm to converge.

The PBC formulation overcame some of the problems with premature failure that were encountered in the DFO

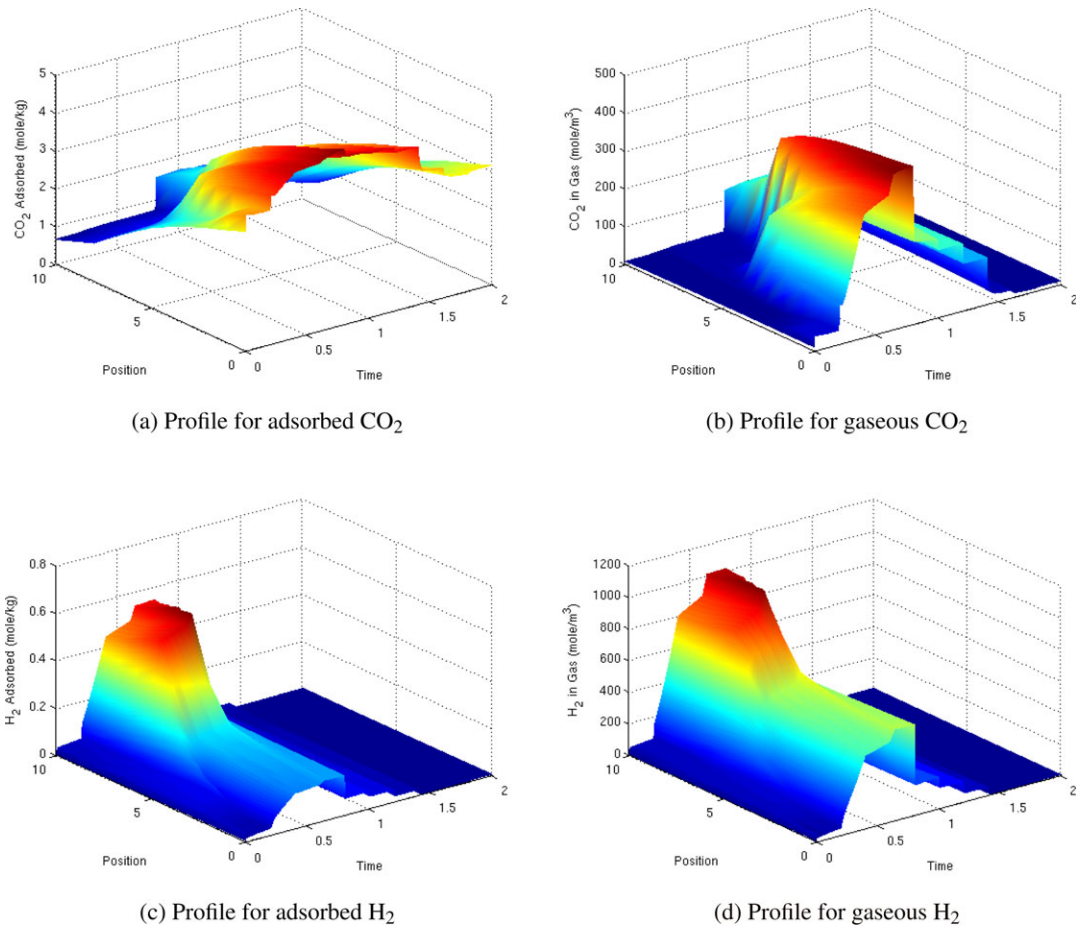

(a) Profile for adsorbed CO_2

(b) Profile for gaseous CO_2

(c) Profile for adsorbed H_2

(d) Profile for gaseous H_2

Figure 7. Mass movement over an entire cycle.

[Color figure can be viewed in the online issue, which is available at wileyonlinelibrary.com.]

approach, leading to lower objective function solutions. However, it converged only with a few combinations of initial conditions and IPOPT options. In all of the PBC cases, we observed the following pattern: after a reasonable number of iterations (10–50), IPOPT would begin to "drift"; the objective function and primal infeasibility would increase, and the dual infeasibility decrease—but not always. In some cases, all three increased. After several iterations of "drifting," the dual infeasibility typically began to increase again. Occasionally, this would be caused by IPOPT taking an "large step," drastically increasing the objective function values and/or primal infeasibility, sometimes entering into a restoration phase. This pattern would repeat until either (1) the maximum number of IPOPT iterations were reached; (2) the numerical integrator reached the maximum number of integration steps per PSA cycle, returned erroneous results and subsequently causing either the IPOPT line search or restoration phase to fail; or (3) IPOPT converged with loose primal and dual tolerances of 10^{-2}. Consistent with IPOPT's convergence properties, this performance is probably due to limited precision of available first derivatives as well as insensitivity to decision variables as a result of smoothed max operators. All gradients require integration of either direct or adjoint sensitivity equations, which are subject to integrator noise. We elaborate on this in the next subsection.

The FH formulation suffered from similar problems when solving the Karush–Kuhn–Tucker conditions. We suspect first derivatives tainted with integrator noise is the primary cause for this behavior. As can be seen in both case studies, neither derivative-based formulation is clearly superior to the other. Although the PBC approach found better solutions in Case Study 1 and Case Study 2A (two components), the FH approach found the best solution in Case Study 2B (five components).

Optimization convergence issues

As previously mentioned, IPOPT suffers from convergence difficulties with the PBC and FH formulations. In most of the case studies, IPOPT failed, but it produced a solution with low primal infeasibilities (PBC and product specification constraints) but large dual infeasibilities (optimality conditions). We suspect that this is caused by an interaction of the max operator used in the smoothing valve and integrator noise introduced when solving the sensitivity equations.

To better understand this phenomenon, let us consider the smoothed check valve on the CoB. If the commanded pressure, P_{ads}, is larger than the pressure at the top of the bed, the check valve is closed. This prevents flow reversal and is required in typical PSA steps, such as pressurization. When the check valve is closed, the solution becomes insensitive to changes in the split fraction parameter β, because there is no flow leaving the bed. The smoothed operator closely matches the max function far away from discontinuity. This means that although some derivative information passes through the smoothed operator near the discontinuity, very little passes through far from the discontinuity. This

Table 6. Multibed Configuration for Continuous Feed and Production

Bed	Slot 1	Slot 2	Slot 3	Slot 4	Slot 5	Slot 6	Slot 7	Slot 8	Slot 9	Slot 10
1A	↑ HR	↑ F & HR	↑ F	↑ F & LP	↓ LP	↓ HR	↓ HR & HP	↓ HP		↑ LP
1B	↓ HR	↓ HR & HP	↓ HP		↑ LP	↑ HR	↑ F & HR	↑ F	↑ F & LP	↓ LP
2A	↑ LP	↑ HR	↑ F & HR	↑ F	↑ F & LP	↓ LP	↓ HR	↓ HR & HP	↓ HP	
2B	↑ LP	↓ HR	↓ HR & HP	↓ HP		↑ LP	↑ HR	↑ F & HR	↑ F	↑ F & LP
3A	↓ HP	↑ LP	↑ HR	↑ F & HR	↑ F	↑ F & LP	↓ LP	↓ HR	↓ HR & HP	↓ HP
3B	↑ F & LP	↑ LP	↓ HR	↓ HR & HP	↓ HP		↑ LP	↑ HR	↑ F & HR	↑ F
4A	↓ HP		↑ LP	↑ HR	↑ F & HR	↑ F	↑ F & LP	↓ LP	↓ HR	↓ HR & HP
4B	↑ F	↑ F & LP	↑ LP	↓ HR	↓ HR & HP	↓ HP		↑ LP	↑ HR	↑ F & HR
5A	↓ HR & HP	↓ HP		↑ LP	↑ HR	↑ F & HR	↑ F	↑ F & LP	↓ LP	↓ HR
5B	↑ F & HR	↑ F	↑ F & LP	↑ LP	↓ HR	↓ HR & HP	↓ HP		↑ LP	↑ HR

Table 7. PSA Equipment Breakdown

Equipment	Capital Cost (TPC)	Power Usage (MW)
Heavy product turbine	\$0.4 M	−1.4
Vaccuum generator	\$6.1 M	5.5
Feed turbine	\$11.7 M	15.5
CO_2 compressor	\$39.3 M	43.7
H_2 compressor	\$7.0 M	5.7
Columns	\$1.4 M	–
Sorbent	\$1.3 M	–
Total	\$67.3 M	38.0

negligible derivative is smaller than the integrator tolerances when commanded pressures (P_{ads}, P_{des}) are much larger than the bed pressures.

Negligible derivative values would explain the observed shortcomings of IPOPT in the case studies. Reformulation of superstructure to avoid these insensitivities could improve optimizer performance with the FH and PBC formulations. Preliminary work suggests that replacing the current control variables with exit velocities may avoid these complications. We leave further study of a reformulated superstructure as future work.

Problem complexity

In the FH formulation, there are fewer decision variables and constraints compared to the PBC formulation, because the long horizon with $N_{fh} = 150–250$ replaces CSS equations. This reduced problem size, however, comes at the price of more expensive optimization iterations. As previously explained, this approach scales better with problem size than the PBC formulation. In Case Study 2B, however, we observed the time per IPOPT iteration was actually larger with the FH formulation. We further explored this issue by measuring CPU time required for both FH and PBC gradients with two control profiles for five gaseous species. These results are shown in Table 13. Before performing the PBC calculations, we simulated the PSA beds to CSS using direct substitution. This eliminated the impact of the boundary condition variables and allows for a more meaningful comparison. The time for simulation to CSS is not included in the results.

Calculating the FH objective function is approximately N_{fh} times more expensive than for PBC, because it involves successive substitution, instead of one simulation pass. Thus, although the gradient calculations with FH formulation are less computationally expensive with five gaseous components, the combined objective function and gradient evaluations are less expensive with the PBC formulation. This is especially true when multiple line search steps are activated, resulting in multiple objective function evaluations per gradient evaluation.

We further explored the impact of problem size on CPU time for both sensitivity methods. In this computational experiment, we increased the number of spatial discretization points for both methods when simulating only two gaseous components. The results are shown in Figure 8. As expected, the adjoint sensitivity computational times grew more slowly

Table 8. Cost of Electricity Comparison

System	COE (\$/MWh)
Optimized PSA	103.1
Dual stage selexol^{TM20}	105.6

Table 9. Termination Conditions

Code	Brief Explanation
1	Converged within termination tolerances BOBYQA: trust region size smaller than tolerance (5×10^{-5}) IPOPT: NLP error less than tolerance (10^{-2})
2	Maximum number of iterations reached BOBYQA: 2500, IPOPT: 3000
3	Solver terminated by user Repeated CVODES error: maximum integration steps reached, producing erroneous obj. func. and gradient results
4	Solver terminated by user Extremely long computational time (order weeks)
5	IPOPT specific error Restoration phase is called at point that is almost feasible… Abort.

with increases in N_{states}. We also fit a model based on complexity analysis to predict computation time.

Here, we considered three major steps for the numerical integration: Jacobian evaluation (via ADOL-C in our implementation), Jacobian factorization (done by CVODES), and solution of the linear system (done by a dense solver in the CVODES). The computational complexity suggests that Jacobian evaluation cost grows linearly with Jacobian size (N_{state}), dense matrix factorization grows cubically with matrix size (N_{state}), and solving a linear system via backsubstitution grows linearly with the system size (N_{sens}). Using this as a guideline, we fit the model given in Eq. 36 to timing data from the computational experiments. The number of Jacobian evaluations (N_{jac}), factorizations (N_{fac}) and linear solves (N_{lin}) were reported by CVODES. All values in the model were scaled by values from the smallest ($N_{state} = 112$) computation experiment. The coefficients for each model are shown in Table 14.

$$t^{scaled} = \alpha N_{jac}^{scaled} N_{state}^{scaled} + \beta N_{fac}^{scaled} (N_{state}^{scaled})^3 + \gamma N_{lin}^{scaled} N_{sens}^{scaled} + \delta \quad (36)$$

Table 13. Gradient Calculation Timings

Control Profile	Sensitivity Method	CPU Min.
Case Study 1 starting point	Direct (PBC)	57.1
	Adjoint (FH)	38.6
Case Study 2B best solution	Direct (PBC)	71.4
	Adjoint (FH)	57.2

The high R^2 values suggest that the simple complexity argument for Eq. 36 mimics the behavior actually seen with the numerical integrator. For adjoint integration, there are two steps. First, the state equations must be integrated forward to obtain state profiles in time. Next, the adjoint equations are integrated backward to obtain derivative information. The poorer fit for the backward adjoint integration model, as indicated by R^2 and diagnostic linear regression plots (not included), suggests a minor computational expense may be missing from the computational time model. Despite this, the models support our expectation that the FH approach (which uses adjoint sensitivity equations) becomes computationally desirable with increased number of spatial discretizations, or more than five components. This is because the FH approach requires fewer optimization variables (N_{opt}) and sensitivity equations (N_{sens}).

Conclusions

We consider a systematic optimization-based formulation for the synthesis and design of novel PSA cycles for CO_2 capture, which can simultaneously produce H_2 and CO_2 at a high purity. Based on a superstructure-based approach and reduced to an OCP with PBCs, this optimization formulation simultaneously determines optimal cycle configurations and design parameters for PSA units.

Our optimization approach integrates ADOL-C, a powerful AD tool, CVODES for the efficient solution of the state, as well as direct and adjoint sensitivity equations and the BOBYQA and IPOPT NLP solvers. Three optimization formulations are considered in this framework: the PBC formulation with PBCs as equality constraints, a DFO formulation

Table 10. Case Study 1 (Two Components)

Approach	Obj. Func (kW h/tonne CO_2)	CPU Time/Iter (h:mm:ss)	Iter	Termination	CO_2 Pur. (%)	CO_2 Rec. (%)
DFO	146.42	0:04:46	566	Converged[1]	**91.90**	90.04
PBC	90.93	0:08:49	202	Restoration[5]	92.02	90.10
FH	94.87	0:19:59	707	Time Term.[4]	92.09	90.09

Table 11. Case Study 2A (Two Components)

Approach	Obj. Func. (kW h/tonne CO_2 captured)	CPU Time/Iter (h:mm:ss)	Iter	Termination	CO_2 Pur. (%)	CO_2 Rec. (%)
DFO	114.31	0:03:28	1215	Converged[1]	92.23	90.01
PBC	83.51	0:10:37	82	Restoration[5]	92.06	90.14
FH	86.45	0:21:09	56	CVODES Term.[3]	92.01	90.59

Table 12. Case Study 2B (Five Components)

Approach	Obj. Func. (kW h/tonne CO_2 captured)	CPU Time/Iter (h:mm:ss)	Iter	Termination	CO_2 Pur. (%)	CO_2 Rec. (%)
DFO	109.04	0:11:29	2500	Max Iter[2]	**90.24**	**89.46**
PBC	89.41	1:00:15	175	Restoration[5]	92.00	90.11
FH	86.81	1:27:52	260	Time Term.[4]	92.06	90.08

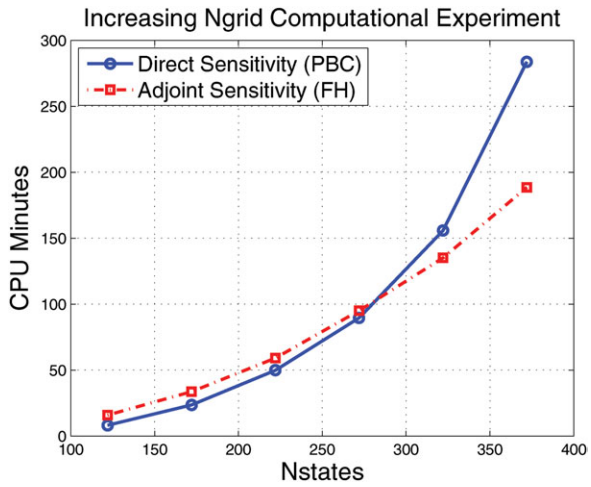

Figure 8. Impact of N_{states} on computational time.

[Color figure can be viewed in the online issue, which is available at wileyonlinelibrary.com.]

with nested solution of the PBCs, and a gradient-based solution with a FH formulation.

These formulations were applied to the binary separation of H_2 and CO_2 at high purity, as well as a larger five component separation. For the binary case, the PBC formulation terminated at a reasonable solution with the least computational cost, especially with a poor initialization. However, the FH formulation ultimately led to the best solution for the five component separation. We also explored the impact of problem size on computational time, ultimately demonstrating that the FH approach becomes more computationally attractive for larger problems.

A number of challenges remain for the optimization strategy. First, as these are nested optimization strategies with embedded ODE solvers, some noisy functions and derivatives still remain even with AD tools coupled to sensitivity equations. We suspect the check valve model creates insensitivities, when no flow is leaving the beds, and we suggest an alternate formulation as future work. As these NLPs are often ill-conditioned, problems still remain for successful convergence. Second, further work is needed to accelerate the solution of the state and sensitivity equations. Clearly, the incorporation of general sparse solvers is essential for ODE and DAE with unstructured Jacobians. Finally, although these nonconvex problems are not large, obtaining a global solution still seems beyond the capability of deterministic global optimization methods. Consequently, careful formulation and problem initialization are essential to avoid premature termination and poor local solutions.

Our optimization methodology also allows the inclusion of physical parameters of the sorbent (e.g., particle diameter, porosity, and metal loading) as decision variables in the optimization problem, as these influence mass transfer

Table 14. Complexity Model Results

Sensitivity Method	α	β	γ	δ	R^2
Direct	−0.93642	0.37003	0.3714	1.3909	0.9914
Adjoint (Forward)	0.39097	0.058655	0.78039	−0.27111	0.9994
Adjoint (Backward)	1.5800	1.1971	1.1923	2.5244	0.92407

Table 15. Optimizer Settings for Case 2

	Case 2A	Case 2B
BOBYQA		
Penalty weight (ρ_{pen})	10^5	10^6
Starting trust region radius	5×10^4	
Final trust region radius	5×10^{-5}	
Variable scaling		
P_{ads} (Pa)	1	
P_{des} (Pa)	10	
α, β, ϕ	5×10^5	
t_s, L_{bed}	2.5×10^4	
Common settings for IPOPT		
μ update strategy	Monotone	
g_{rec}, g_{pur} scaling	100	
t_s scaling	1/60	
L_{bed} scaling	1/10	
Problem scaling	Automatically done by IPOPT	
IPOPT (PBC)		
User slack $g(\bullet)$	Yes	Yes
$\bar{z}(x,0) \geq 0$ constraint	No	Yes
IPOPT (FH)		
User slack $g(\bullet)$	No	No

[User slack $g(\bullet)$ refers to the user manually adding a slack variable thus converting the inequality constraints to equality constraints. Alternately, the $g(\bullet)$ can be directly specified as an inequality constraint in IPOPT.]

models and isotherms. In addition, the distribution of layered sorbent models (as in Ref. 11) can also be incorporated directly as a set of decisions. In the future, we also plan to develop reduced order models drawn from computational chemistry to integrate material models within the optimization formulation.

Moreover, hybrid separation processes also offer a benefit to CO_2 separation. Kumar and Shah[22] considered the combination of PSA with cryogenic distillation. Hybrid processes that combine PSA with membrane processes have also been proposed.[23,24] In future work, we look forward to extending our superstructure formulation to consider integration with these separations processes as well.

Acknowledgments

This work was completed with assistance from the National Energy Technology Laboratory (NETL). The authors are grateful to David Miller, who acted as the primary liaison with NETL, as well as James Black and Michael Matuszewski, who provided details for Case 2[20] necessary for scale-up and costing.

This report was prepared as an account of work sponsored by an agency of the United States Government. Neither the United States Government nor any agency thereof, nor any of their employees, makes any warranty, express or implied, or assumes any legal liability or responsibility for the accuracy, completeness, or usefulness of any information, apparatus, product, or process disclosed, or represents that its use would not infringe privately owned rights. Reference herein to any specific commercial product, process, or service by trade name, trademark,

Table 16. Additional Case Study Data

Feed pressure	51 bar	
Feed temperature	308 K	
N_{stages} for H_2 product compressor	3	
N_{stages} for CO_2 product compressor	6	
N_{stages} for feed turbine	∞	
P_{out} for H_2 product compressor	31 bar	
P_{out} for CO_2 product compressor	150 bar	
Feed Composition (mol %)	Case 1 & Case 2A	Case 2B
y_{H_2}	0.58	0.5650
y_{CO_2}	0.42	0.4200
y_{CO}	–	0.0077
y_{CH_4}	–	0.0009
y_{N_2}	–	0.0064

manufacturer, or otherwise does not necessarily constitute or imply its endorsement, recommendation, or favoring by the United States Government or any agency thereof. The views and opinions of authors expressed herein do not necessarily state or reflect those of the United States Government or any agency thereof.

Notation

Latin letters

$a_c^i,\ldots,d_c^i$ = specific heat correlation coefficient for species i, J/(mol K,…,J mol K^4)
b_L = generic lower bounds
b_{mi} = Langmuir isotherm coefficients for species i, site m, 1/Pa
b_U = generic upper bounds
$C_{a,i}$ = concentrations of species i exiting adsorption bed, mol/m^3
$C_{d,i}$ = concentrations of species i exiting desorption bed, mol/m^3
$C_{feed,i}$ = concentrations of species i in feed stream, mol/m^3
C_i = gas-phase concentration for species i, mol/m^3
C_{pg}^i = ideal gas specific heat for species i, J(mol K)
C_{ps} = sorbent specific heat, (711.75), J/(kg K)
d_p = sorbent particle diameter, (1.49×10^{-3}), m
E = Net specific energy for entire system, kW h/mol CO_2
$E^{(k)}$ = Energy used/produced by compressor/turbine k, kW h/m^2
f = right-hand side of ODEs
F_i = feed flux, mol/(m^2 s)
$g(\bullet)$ = inequality constraints
h = entalphy, J/m^3
$h(\bullet)$ = equality constraints
ΔH_i^{ad} = enthalpy of adsorption for species i, J/mol
k_i = effective mass-transfer coefficient for species i, 1/s
k_{mi}^1 and k_{mi}^2 = isotherm coefficient correlations for species i, site m, mol/kg and mol/(kg K)
k_{mi}^3 and k_{mi}^4 = isotherm coefficient correlations for species i, site m, mol/kg and K
L_{bed} = length (aka height) of PSA bed (0.5–50.0†, m
M_w^i = molecular weight for species i, g/mol
N_{aux} = number of auxillary PSA eqns (12)
N_{comp} = number of gas components (2 or 5)
N_{fac} = number of Jacobian factorizations
N_{fh} = number of direct subs in fixed horizon (200)
N_{grid} = number of bed discretization grid elements 11
N_{jac} = number of Jacobian evaluations
N_{fac} = number of linear system solves
N_{sens} = number of sensitivity eqns
N_{slot} = number of slots (aka steps) in PSA cycle (5)
N_{state} = number of state variables
P = pressure, atm or Pa
p = vector of parameters (used in sensitivity eqns)
P_{ads} = adsorption pressure (control variable; $\geq 4.93^\dagger$), atm*
P_{des} = desorption pressure (control variable; $\geq 10^{-4\dagger}$), atm*
P_{in}^k = inlet pressure for compressor/turbine k, atm
P_{out}^k = outlet pressure for compressor/turbine k, atm
q_i = actual sorbent loading for species i, mol/kg
q_i^* = equilibrium sorbent loading for species i, mol/kg
q_{mi}^s = langmuir isotherm coefficients for species i, site m, mol/kg
R = ideal gas constant (8.314), J/(mol K)
r = ratio of gradients (used in flux limiter)
r' = smoothed ratio of gradients (used in flux limiter)
S = sensitivity matrix (used in sensitivity eqns)
T = temperature, K
t = time dimension, s
t_s = length of step in cycle (5–500†), s
T_w = ambient (aka wall) temperature (298), K
U_A = vessel wall heat transfer coefficient times area, (0.2839), J/(s K m^3)
v = gas velocity, m/s
v_a = gas velocity exiting adsorption bed, m/s
v_d = gas velocity exiting desorption bed, m/s
v_{feed} = feed gas velocity (0.5), m/s
x = bed height dimension, m
z = generic differential state variable

*Units are implemented as Pa for DFO approach and atm for PBC and FH approaches.
†Variable bounds used for PBC and FH approaches.

Greek letters

α = bottom reflux fraction (control variable;• 0–1†)
β = top reflux fraction (control variable; (0–1†)
ε = constant for smoothing (10^{-2})
ε_b = internal bed void fraction (0.37)
ε_{CSS} = CSS tolerance for direct substitution (10^{-2} or 10^{-3})
ε_t = external void fraction (0.71)
η^k = efficiency for compressor k (0.8)
γ = adiabatic index (1.4)
λ = adjoint variables (used in sensitivity eqns)
μ = gas viscosity (1.2021×10^{-5}) kg/m s
ϕ = feed fraction (control variable; 0–1†)
Φ = objective function, kW h/tonne CO_2 captured
φ = flux limiter function
ψ = vector of objective function and constraints
ρ_s = sorbent density (544.64), kg/m^2

Literature Cited

1. IEA/WEO. *World Energy Outlook 2006. Tech. Rep. Paris*, France: International Energy Agency, 2006.
2. Schell J, Casas N, Mazzotti M. *Pre-combustion CO_2 capture for IGCC plants by an adsorption process. Energy Procedia. 2009;1(1):655–660*. In: *Proceedings of the 9th International Conference on Greenhouse Gas Control Technologies (GHGT-9)*, Washington, DC, USA 16–20 November, 2008.
3. Ho MT, Allinson GW, Wiley DE. Reducing the cost of CO_2 Capture from flue gases using pressure swing adsorption. *Ind Eng Chem Res*. 2008;47(14):4883–4890.
4. Rajasree R, Moharir AS. Simulation based synthesis, design and optimization of pressure swing adsorption (PSA) processes. *Comput Chem Engi*. 2000;24(11):2493–2505.
5. Nikolić D, Giovanoglou A, Georgiadis MC, Kikkinides ES. Generic modeling framework for gas separations using multibed pressure swing adsorption processes. *Ind Eng Chem Res*. 2008;47(9):3156–3169.
6. Nikolić D, Kikkinides ES, Georgiadis MC. Optimization of multibed pressure swing adsorption processes. *Ind Eng Chem Res*. 2009;48(11):5388–5398.
7. Agarwal A, Biegler LT, Zitney SE. Superstructure-based optimal synthesis of pressure swing adsorption cycles for precombustion CO_2 capture. *Ind Eng Chem Res*. 2010;49(11):5066–5079.
8. Vetukuri SRR, Biegler LT, Walther A. An inexact trust-region algorithm for the optimization of periodic adsorption processes. *Ind Eng Chem Res*. 2010;49(23):12004–12013.
9. Daeho Ko RS, Biegler LT. Optimization of pressure swing adsorption process using zeolite 13X for CO_2 sequestration. *Ind Eng Chem Res*. 2003;42(2):339.
10. Daeho Ko RS, Biegler LT. Optimization of pressure swing adsorption and fractionated vacuum pressure swing adsorption processes for CO_2 sequestration. *Ind Eng Chem Res*. 2005;44:8084–8094.
11. Jiang L, Fox VG, Biegler LT. Simulation and optimal design of multiple-bed pressure swing adsorption systems. *AIChE J*. 2004; 50(11):2904–2917.
12. Vetukuri SRR. *Advanced Optimization Strategies for Periodic Adsorption Processes*. Ph.D. thesis, Carnegie Mellon University, 2011.
13. Balakrishna S, Biegler LT. Targetting strategies for the synthesis and heat integration of nonisothermal reactor networks. *Ind Eng Chem Res*. 1992;31(9):2152–2160.
14. Biegler LT, Grossmann IE, Westerberg AW. *Systematic Methods of Chemical Process Design*. Upper Saddle River, NJ: Prentice Hall, 1997.
15. Jiang L, Fox VG, Biegler LT. Simulation and optimization of pressure swing adsorption systems for air separation. *AIChE J*. 2003;49(5):1140–1150.
16. Hindmarsh AC, Serban R. *User Documentation for CVODES v2.6.0*. Livermore, CA: Center for Applied Scientific Computing, Lawrence Livermore National Laboratory, 2009.
17. Griewank A, Juedes D, Utke J. ADOL-C: a package for the automatic differentiation of algorithms written in C/C++. *ACM Trans Math Softw*. 1996;22:131–167.
18. Wächter A, Biegler L. On the implementation of a primal–dual interior point filter line search algorithm for large-scale nonlinear programming. *Math Program*. 2006;106(1):25–57.

19. Powell M. The BOBYQA algorithm for bound constrained optimization without derivatives. *Tech. Rep*. DAMTP 2009/NA06. Department of Applied Mathematics and Theoretical Physics, University of Cambridge, Cambridge, UK, 2009.
20. Black J, et al. Cost and performance baseline for fossil energy plants—Vol. 1: Bituminous coal and natural gas to electricity. *Tech. Rep*. National Energy Technology Laboratory, Morgantown, WV, 2010.
21. Agarwal A, Biegler LT, Zitney SE. A superstructure-based optimal synthesis of PSA cycles for post-combustion CO_2 capture. *AIChE J*. 2010;56(7):1813–1828.
22. Kumar R, Shah M. Adsorption based hybrid technology to recover CO_2. *Tech. Rep*. In: Paper 404f presented at Annual AIChE Meeting, Nashville, TN, 2009.
23. Nikolakis V. HY2SEPS EU Framework 6 Project. *Tech. Rep*. 2009. Available at: http://hy2seps.iceht.forth.gr.
24. Picioccio K, Zagoria A. Options for improving hydrogen network operations. *Tech. Rep*. National Petrochemical & Refiners Association, In: 107th NPRA Annual Meeting, Houston, TX, 2009.

Manuscript received Jun. 17, 2012, and revision received Sept. 1, 2012.